# Electromagnetics-Aware Path for UAV-Based Near-Field Antenna Measurements Implemented With a High Dynamic Range SDR

*Original*
Electromagnetics-Aware Path for UAV-Based Near-Field Antenna Measurements Implemented With a High Dynamic Range SDR / Ciorba, L., Paonessa, F., Righero, M., Giordanengo, G., Addamo, G., Vecchi, G., Virone, G.. - In: IEEE TRANSACTIONS ON INSTRUMENTATION AND MEASUREMENT. - ISSN 0018-9456. - 73:(2024). [10.1109/tim.2024.3476517]

*Publisher:*
IEEE

*Published*
DOI:10.1109/tim.2024.3476517

# Electromagnetics-Aware Path for UAV-Based Near-Field Antenna Measurements Implemented With a High Dynamic Range SDR

Lorenzo Ciorba, Fabio Paonessa, *Member, IEEE*, Marco Righero, Giorgio Giordanengo,
Giuseppe Addamo, *Member, IEEE*, Giuseppe Vecchi, *Life Fellow, IEEE*,
and Giuseppe Virone, *Senior Member, IEEE*

***Abstract*— An electromagnetics-aware path for drone-based near-field (NF) antenna measurements is implemented in an outdoor experimentation. This technique allows us to significantly reduce the scan duration with respect to a standard half-wavelength NF scanning, using knowledge of the antenna under test (AUT) electrical size only. The validity of our approach is corroborated with planar outdoor NF measurements performed with an untethered drone transmitting at 750 MHz. To deal with the absence of phase coherence, the phase information is retrieved from a reference antenna, while a software-defined radio (SDR) having four super-heterodyne receiving channels is used to properly sample the high-dynamic signals resulting from the large scanning surface.**

***Index Terms*— Antenna measurements, near-field to far-field transformation (NFT), reduced order model, software-defined radio (SDR), unmanned aerial vehicle (UAV).**

## I. INTRODUCTION

IN RECENT years, unmanned aerial vehicles (UAVs) opened up new possibilities for the antenna measurement community by facilitating outdoor operations even in complex environments [1], [2]. Their use is widely documented in literature as a solution for in situ far-field (FF) testing [3], [4], [5], [6], and in 2021 a UAV-based procedure was added in the IEEE recommended practice for antenna measurements [7].

Thanks to their affordability and flight precision, unmanned rotorcrafts such as quadcopters and multicopters are particularly suitable for in situ measurements of big antennas that cannot be placed inside an anechoic chamber, or for which the environment cannot be adequately reproduced indoor. This is the case, for instance, of modern radio telescopes such as the square kilometer array (SKA) [8], the low frequency array (LOFAR) [9], [10] and the electronic multibeam radio astronomy concept (EMBRACE) [11], [12].

To both comply with the maximum flight height allowed by regulations (120 m in Europe, 400 feet in USA) and ensure safe operability in complex scenarios, near-field (NF) measurements represent the natural evolution of UAV antenna testing. Standard NF techniques generally employ automated scanners (e.g., planar, cylindrical, or spherical) and a NF to FF transformation (NFT) to predict the FF antenna behavior [13]. UAV-based NF measurements are also reported in [14], [15], and [16]; however, their applicability is still not consolidated for the reasons summarized below.

First, in the absence of a wired link between the UAV and the ground equipment, the receiver cannot share the same frequency reference as the transmitter (i.e., they are not phase-locked); hence, the measured phase will rapidly drift even if the probe is stationary with respect to the antenna under test (AUT). Magnitude-only (phaseless) transformations were proposed for UAV-based measurements [14]; however, this approach turns to a nonlinear and nonconvex problem where local minima can occur. To achieve phase coherence, fiber-optic links were used both outdoor [15] and indoor [16]. These approaches exploit a physical link to transfer the RF signal through RF-over-fiber technology (RFoF). However, the presence of the tether represents a constraint for the UAV, which is forced to execute mainly vertical flights (e.g., planar, or cylindrical). A further method, applicable with a receiving AUT, consists in measuring the relative phase between the AUT and a reference antenna [7, pp. 91–92], [17] so that the phase drift of the UAV generator is completely removed. This eliminates the necessity of a wired link but requires a multiport vector acquisition system.

Second, differently from standard NF scanners where the probe always points toward the AUT (in cylindrical and spherical scanning, typically), in UAV-based measurements the probe orientation coincides with the aircraft attitude (i.e., the state of the three angles that describe the spatial orientation of the aircraft, namely yaw, pitch, and roll), which in turn

---

Received 26 July 2024; accepted 17 September 2024. Date of publication 9 October 2024; date of current version 21 October 2024. The Associate Editor coordinating the review process was Dr. Yuto Kato. *(Lorenzo Ciorba and Fabio Paonessa are co-first authors.) (Corresponding author: Fabio Paonessa.)*

Lorenzo Ciorba was with the Institute of Electronics, Information and Telecommunications Engineering, Consiglio Nazionale delle Ricerche, 10129 Turin, Italy. He is now with the Institute of Applied Physics, University of Bern, 3012 Bern, Switzerland (e-mail: lorenzo.ciorba@unibe.ch).

Fabio Paonessa, Giuseppe Addamo, and Giuseppe Virone are with the Institute of Electronics, Information and Telecommunications Engineering, Consiglio Nazionale delle Ricerche, 10129 Turin, Italy (e-mail: fabio.paonessa@cnr.it; giuseppe.addamo@cnr.it; giuseppe.virone@cnr.it).

Marco Righero and Giorgio Giordanengo are with the Advanced Computing, Photonics and Electromagnetics, LINKS Foundation, 10138 Turin, Italy (e-mail: marco.righero@linksfoundation.com; giorgio.giordanengo@linksfoundation.com).

Giuseppe Vecchi is with the Department of Electronics and Telecommunications, Politecnico di Torino, 10129 Turin, Italy (e-mail: giuseppe.vecchi@polito.it).

Digital Object Identifier 10.1109/TIM.2024.3476517

depends on its motion. For this reason, probe compensation becomes necessary. Moreover, the dynamic of the measured signal can significantly increase with respect to the same scanning strategy performed with a standard scanner system. In fact, even in the case the probe is scarcely directive (e.g., a half-wavelength dipole), its radiation pattern can be considerably altered when mounted on the UAV [18], and nulls can appear in the observation direction of the AUT. Rotorcrafts can arbitrarily vary the heading angle; this capability can be exploited to keep the horizontal pointing direction locked to the AUT, but it only helps in some flight configurations and partially mitigates the problem since neither pitch nor roll can be arbitrary. The strong coupling between the UAV and the onboard probe, especially at low frequencies, also limits the applicability of gimbals to accomplish the continuous adjustment of the pointing direction.

Finally, the measurement time required by a standard NF scanning can be prohibitive for close range UAVs due to the normally required sampling density ($\lambda/2$ or less) [13, p. 23]. For example, a half-wavelength planar scanning at 350 MHz over a station of the SKA, whose diameter is 40 m [6], gives a 5 km long path that requires a flight of about an hour.

Antenna characterization using sparse scanning and minimum set of NF samples [19], [20], [21], [22], [23] is documented in literature, with a focus on minimizing the number of samples needed to specify the radiated field. To the best of the authors' knowledge, there is no application of techniques to reduce the number of scanning acquisitions in UAV measurements that explicitly consider the length of the flight and are experimentally validated.

The main novelty of this article is the implementation of a UAV-based NF measurement that uses an electromagnetics-aware path and a multichannel receiver based on a software-defined radio (SDR). Our approach is based on the combined use of a factorized representation of the radiation operator to determine the waypoints that shall be reached by the UAV, of a standard optimization algorithm to determine the shortest path visiting each of the waypoints and of an inverse-source based NFT. Preliminary results were shown in [24] and [25].

Here, the path generation algorithm is presented and the measured results from an outdoor experimental campaign at 750 MHz, including the NFT, are thoroughly discussed.

A further novel aspect is the usage of a multiport SDR with high dynamic range (superheterodyne-based). With respect to commonly employed vector network analyzers (VNAs), SDRs offer scalability and modulation/demodulation capability. The latter opens up, in a future perspective, new possibilities for over-the-air (OTA) or multiple-input multiple-output (MIMO) characterization of complex antenna systems with UAVs. So far, the use of SDRs for antenna measurements has been mostly documented inside anechoic chambers employing homodyne receivers with limited dynamic range [16], [26], [27].

It is worth mentioning that although this work concerns UAVs, an EM-aware path approach can be generalized to other scenarios in which different positioners are used.

This article is organized as follows. Section II describes the EM-aware path derivation in the case of a horizontal planar outdoor scenario where the scanning time is reduced by four times with respect to its respective standard $\lambda/2$ planar scanning. Numerical tests are performed to assess the scalability of the method with respect to the size of the AUT and to compare it with more traditional approaches, such as a $\lambda/2$ raster scan and a scan along a spiral path with $\lambda/2$ pitch. Section III presents the SDR receiving system addressing the aspects of dynamic range and synchronization with the UAV data. Section IV reports the experimental setup and phase retrieval from reference antenna. Finally, Section V discusses the results comparing them with simulations, FF measurements and a standard $\lambda/2$ planar scanning.

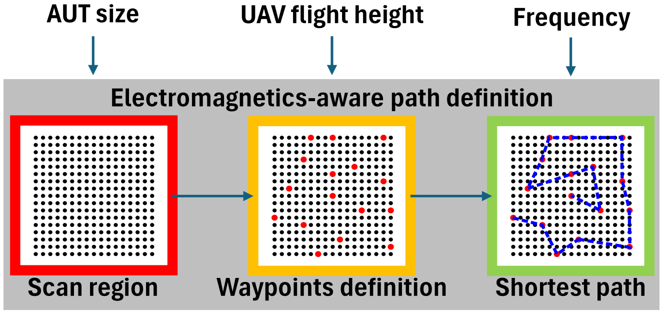

Fig. 1. Block diagram of the EM-aware path generation.

## II. EM-Aware Path Calculation

A factorized representation of the radiation operator underpins the proposed strategy to determine the waypoints that shall be reached by the UAV to acquire the needed amount of information [20]. The approach is based on the inverse source NFT using equivalent currents that produce the AUT field. Such a technique is able to deal with an irregular grid of measurement points, for example, a cloud of points coming from UAV-based measurements.

The algorithm rationale is illustrated in the high-level block diagram of Fig. 1 and the more detailed flowchart of Fig. 2. First, the principles of the inverse source technique are briefly recalled (see red frames). A virtual surface enclosing the AUT is defined, then, equivalent electric and magnetic currents representing the AUT field are defined over this surface. By enforcing a null field inside the virtual surface, the currents are directly related to the tangent electric and magnetic fields [28]. The virtual surface is then discretized through an appropriate tessellation, and Rao–Wilton–Glisson (RWG) [29] basis functions are defined over it. In this way, each current is expanded as a linear combination of RWGs through unknown coefficients.

As far as the EM-aware path computation is concerned, a matrix $\boldsymbol{B}$ is built containing samples of the radiator operator evaluated between $L$ source points $\underline{r}'_\ell$ distributed around the volume of the AUT and $M$ target points $\underline{r}_m$ distributed to scan the region of interest where the UAV could fly

$$B_{m\ell} = \frac{e^{-ik_0\|\underline{r}_m-\underline{r}'_\ell\|}}{\|\underline{r}_m-\underline{r}'_\ell\|}. \tag{1}$$

It should be noted that columns and rows of $\mathbf{B}$ are related to equivalent source position and measurement points,

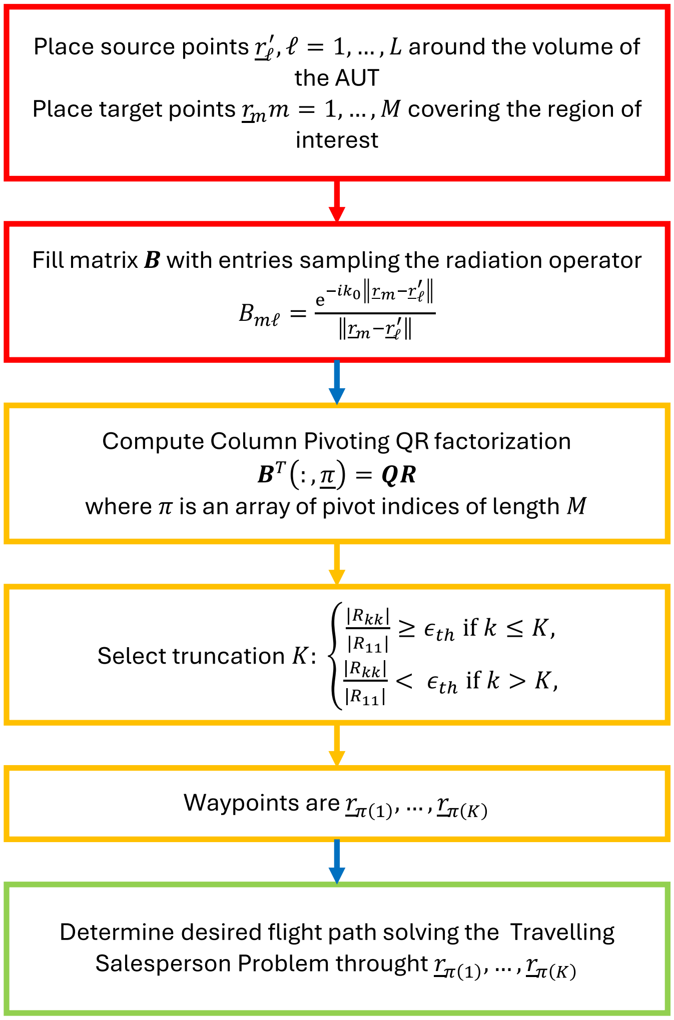

Fig. 2. Flowchart of the EM-aware path generation algorithm.

respectively. Hence, undersampling the measurement points is equivalent to subsample the rows of $\mathbf{B}$.

For this purpose, a truncated CPQR factorization (yellow frames) is evaluated for the transpose of $\boldsymbol{B}$ in order to extract the most electromagnetically significant waypoints [30], [31]

$$\boldsymbol{B}^T(:,\underline{\pi}) = \boldsymbol{QR} \tag{2}$$

where $\underline{\pi}$ is an array of pivot indices of length $M$. Given a threshold $\epsilon_{\text{th}}$, we determine the number of waypoints $K$ looking at the element of the matrix $\boldsymbol{R}$

$$K\colon \begin{cases} \dfrac{|R_{kk}|}{|R_{11}|} \geq \epsilon_{\text{th}}, & \text{if } k \leq K \\ \dfrac{|R_{kk}|}{|R_{11}|} < \epsilon_{\text{th}}, & \text{if } k > K. \end{cases} \tag{3}$$

The waypoints are then the $K$ target points $\underline{r}_{\pi(1)}, \dots, \underline{r}_{\pi(K)}$.

The shortest route connecting all the $K$ waypoints is found (green frames) solving the traveling salesperson problem, and the path for the UAV flight is defined. The AUT is then characterized from samples acquired along this path. This means that the matrix used to enforce equality between the field radiated by the currents and the measured samples is computed considering points along the EM-aware path.

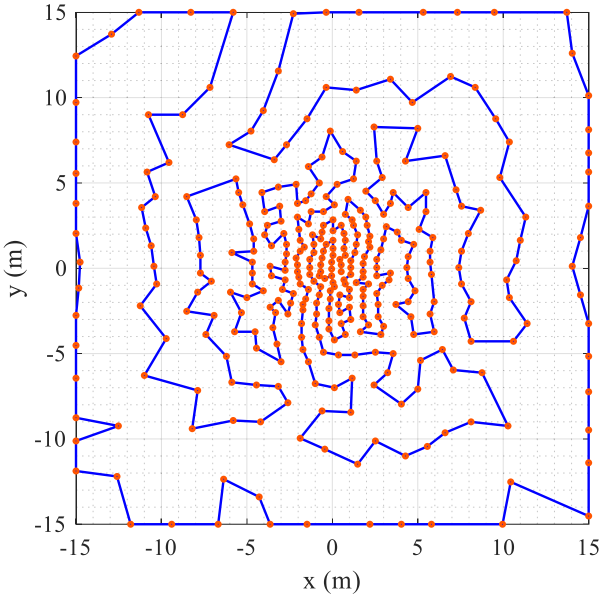

Fig. 3. Map in the $xy$ plane of 350 most electromagnetically significant waypoints (orange dots) and shortest path connecting them (blue line) determined for a two-element array having a characteristic size of $8.5\lambda$ at 750 MHz. Starting and arrival waypoints located close to the origin.

Fig. 3 shows the EM-aware planar path for a two-element array having an overall size of $8.5\lambda$ at 750 MHz, computed at a height of 4 m ($\approx 10\lambda$) (orange markers highlighting the 350 most electromagnetically significant waypoints) with $\epsilon_{\text{th}} = 10^{-3}$. The figure highlights that the EM-aware path provides a dense sampling near zenith, whereas greater spacing between samples is allowed for large values of the zenith angle. This is also in agreement with other results in [32], [33], and [34].

Rigorously speaking, it should be noted that only the most electromagnetically significant waypoints (red dots in Fig. 3) must be sampled. This means that all the other points acquired during the UAV flight (when the UAV is moving between two consecutive waypoints) represent redundant information. On the other hand, the UAV is not capable of precisely follow the programmed path, that is, the acquired samples will lie close to the programmed ones. However, this inaccuracy is compensated for by the strong unavoidable oversampling that occurs between two consecutive waypoints.

Fig. 4 shows the path length of the EM-aware path strategy and of a spiral scanning in relation to the length of an equivalent standard half-wavelength NF acquisition. It should be reminded that once the desired angular validity of the NFT is chosen, the size of the NF scan only depends on the distance between AUT and probe [35], in this case equal to 4 m ($\approx 10\lambda$). As shown in the figure, the amount of time saved by adopting the EM-aware path strategy ranges from ~35% to ~90% of the time required by a standard $\lambda/2$ planar raster, depending on the AUT electrical size, flight height, chosen angular validity and truncation threshold $\epsilon_{\text{th}}$, and compares favorably with the results of the spiral scanning, which is constant around 20%.

Finally, we studied how the truncation threshold $\epsilon_{\text{th}}$ affects the accuracy of the reconstructed FF. We considered a testbed

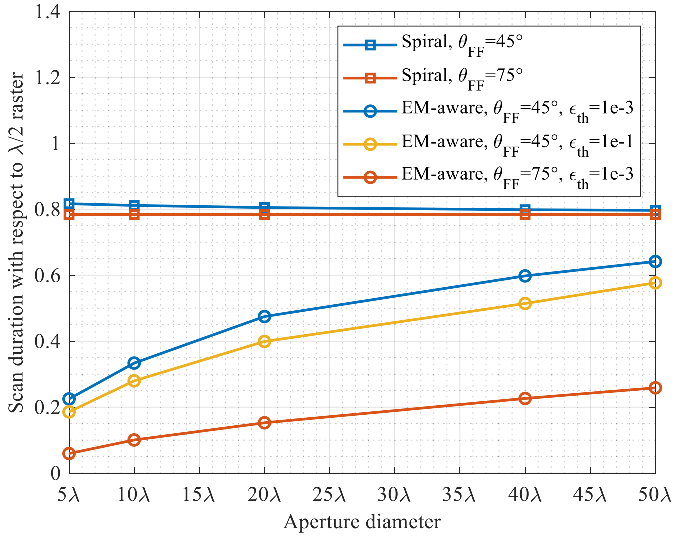

Fig. 4. Overall scan length of an EM-aware path and of a spiral path with respect to the standard planar NF $\lambda/2$ raster, as a function of the AUT electrical size. In the legend, $\epsilon_{\text{th}}$ denotes the truncation threshold, whereas $\theta_{\text{FF}}$ the angular validity of the NFT.

consistent with the experimental setup in Section IV-B. It features two antennas 2.5 m apart simulated at 750 MHz with an in-house method of moments (MoMs) code [36], considering a square 30-m wide scanning area at a flight height of 4 m. We evaluated the FF pointwise error as

$$\Delta_{\text{FF}}(\theta,\phi) = 20\log_{10}\left(\text{FF}^{\text{ref}}\right) - 20\log_{10}\left(\text{FF}^{\text{rec}}\right) \tag{4}$$

that is, the logarithmic difference ([37]) between the magnitude of the FF obtained from the MoM solution $\text{FF}^{\text{ref}}(\theta,\phi)$, and the magnitude of FF obtained applying the inverse-source method to NF samples (from the same MoM code) at the location determined by the proposed CPQR-based algorithm, $\text{FF}^{\text{rec}}(\theta,\phi)$. We then computed the mean absolute error as

$$\Delta_{\text{FF}} = \frac{1}{M^{\text{FF}}} \sum_{\{|\theta_n|\le\theta_{\text{FF}}\}} |\Delta_{\text{FF}}(\theta_n,\phi_n)| \tag{5}$$

where $\theta_{\text{FF}}$ is the validity angle imposed by the limited scan area and $(\theta_n,\phi_n)$ are direction, where the FF is evaluated and $M^{\text{FF}}$ is the number of directions $(\theta_n,\phi_n)$ such that $|\theta_n| \le \theta_{\text{FF}}$. Fig. 5(a) shows the scaling of $\Delta_{\text{FF}}$ (blue line) and of the number of waypoints $K$ (orange) as a function of the truncation threshold $\epsilon_{\text{th}}$. The truncation value $\epsilon_{\text{th}} = 10^{-3}$ (see vertical dotted line) adopted for the path implemented in this work (Fig. 3, 350 waypoints) provides a negligible error of ∼0.06 dB. A higher truncation level of 0.1 would instead provide only ∼200 waypoints and a reconstruction error of ∼0.4 dB. Further details about the relationship between the FF error $\Delta_{\text{FF}}$ and the length of the path through the waypoints identified with (2) and (3) are shown in Fig. 5(b).

## III. SDR-BASED RECEIVER

The adopted device is an Ettus Research X310 [38] USRP[1] with two TwinRX [39] daughterboards; this configuration provides four coherent receiving channels and can be further scaled up.

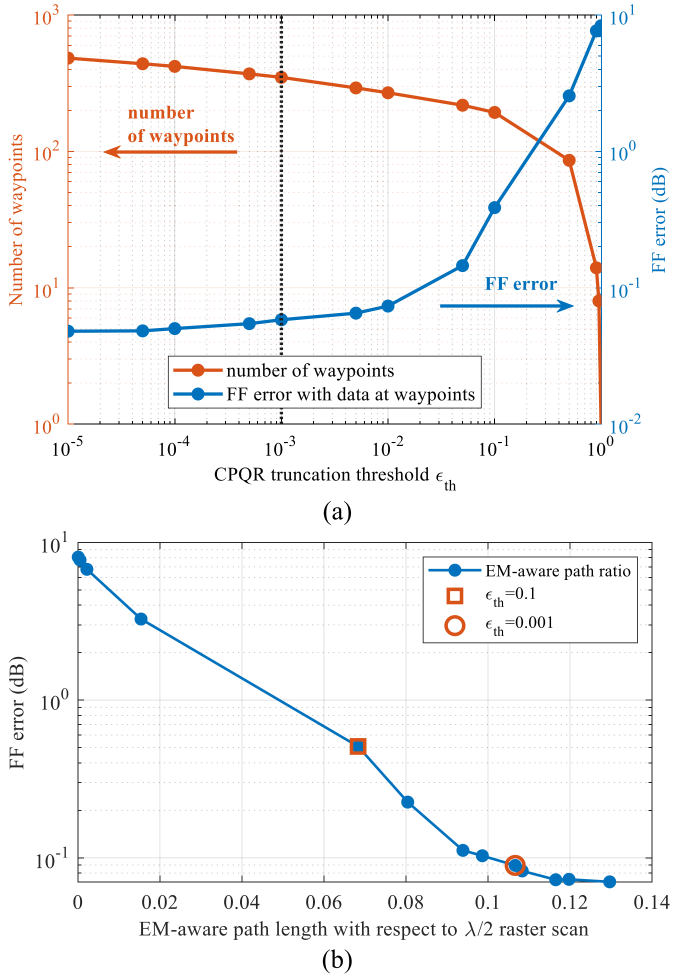

(a)

(b)

Fig. 5. (a) FF error $\Delta_{\text{FF}}$ and number of waypoints as a function of the truncation threshold $\epsilon_{\text{th}}$ with the simulative testbed. (b) FF error $\Delta_{\text{FF}}$ as a function of ratio of the EM-aware path length with respect the length of a $\lambda/2$ planar raster, with cases corresponding to $\epsilon_{\text{th}} = 0.1$ and $\epsilon_{\text{th}} = 0.001$ marked with a square and a circle, respectively.

The hardware architecture of the X310 incorporates two daughterboard slots with a baseband bandwidth of 160 MHz each. The radio also contains a GPS disciplined oscillator (GPSDO), which provides timestamp capability with ±50 ns of synchronization accuracy to UTC time. In other words, the data stream incorporates the timestamp for each sample. This feature is particularly important since the UAV data and the RF data are sampled asynchronously. To allow the postprocessing, the collected RF data are merged with the UAV position data by a linear interpolation of the latter at the RF sample time.

As far as the daughterboards are concerned, one TwinRX implements two independent superheterodyne receivers tunable from 10 MHz to 6 GHz with 80 MHz of instantaneous bandwidth each. The daughterboards can share the local oscillator (LO) across different boards, thus enabling coherent and phase-aligned measurements. Configurable attenuation and amplification stages allow to achieve the maximum dynamic range of 110 dB at 2.4 GHz [39]. It should be noted, however, that the maximum value can be achieved by dynamically

---

[1] Trademarked.

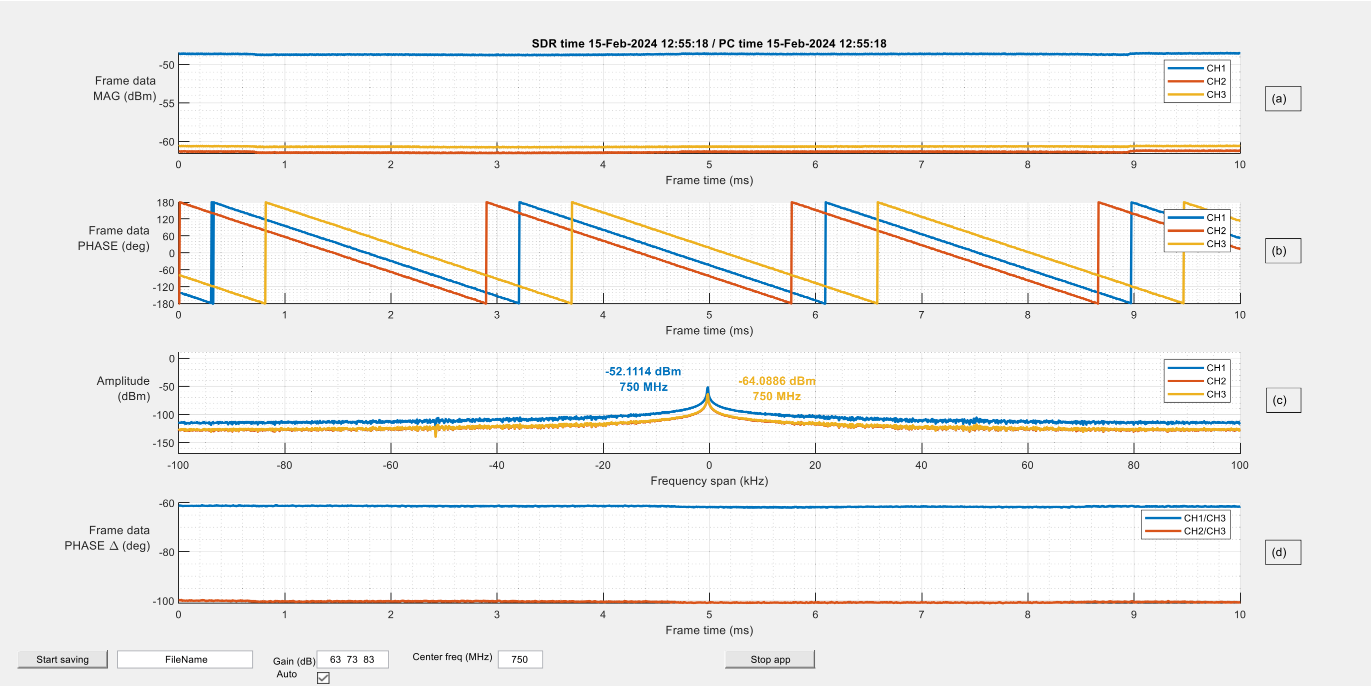

Gain (dB) 63 73 83

Auto ☑

Center freq (MHz) 750

Fig. 6. Screenshot of the developed user interface during a laboratory test in which three coherent continuous waveforms were captured by three separate SDR channels. From top to bottom: (a) magnitudes and (b) phases of the complex signals acquired within one frame for channel 1 (blue), 2 (orange), and 3 (yellow). (c) Power spectra (the curve of CH2 is hidden by CH3). (d) Phase difference between CH1 and CH3 (blue curve) and between CH2 and CH3 (red curve) within one frame. The standard deviation of the phase difference was 0.21° (CH1/CH3) and 0.27° (CH2/CH3). Additional buttons and text boxes to set gain, center frequency, and start/stop acquisition.

adjusting the total channel gain (in the range 0–93 dB). This operation introduces a discontinuity in the measured phase, which must be detected and compensated by the acquisition software. Within one value of gain, laboratory tests under different conditions highlighted a maximum dynamic range of about 70 dB where linearity was verified. Moreover, the measured standard deviation of the phase difference between coherent waveforms was within 0.3° see Fig. 6).

The SDR samples the signals with a default rate of 200 MS/s, while a decimation filter can reduce the sample rate by a factor of 1–1024. The complex samples are then grouped in frames of arbitrary length and streamed one frame at a time through a digital interface.

To communicate with the device, we developed a custom application with MATLAB.[2] The program allows to set the main parameters of the radio (e.g., center frequency, gain, and sampling rate), acquire the data and store them on the hard drive. Real-time data processing functionalities are also available; in particular, a fast Fourier transform (FFT) is performed in real-time to show the acquired signals in terms of magnitude, phase, and spectral power distribution (Fig. 6).

Within the scope of this work, the test-source transmitted a continuous wave (CW) signal. With such a narrow-band signal, a decimation factor of 1000 was used to save throughput demand. This value gives a measured bandwidth of 200 kHz, which is still enough to account for misalignments of the center frequencies between the test-source and the SDR, and for possible modulations induced by the vibrations of the UAV [40]. The frame duration was set to 10 ms (2000 samples per frame), therefore, the distance traveled within a frame is $\lambda/40$ assuming a UAV speed of 1 m/s. A smaller frame duration (e.g., 1 ms) could in principle be set, but this would have produced excessive fragmentation of the data stream, degrading the transmission speed. The frame data were acquired by our software at the rate of 100 fps; however, to save computational and storage demand, only 6 fps were kept while the others were discarded. For each valid frame, the complex FFT together with the associated timestamp was stored on the hard drive for postprocessing. This corresponds to a nominal sampling density of about $\lambda/2.4$ if the UAV moves at 1 m/s.

## IV. MEASUREMENT SETUP

### A. UAV

We employed a multicopter equipped with a programmable frequency synthesizer and a dipole antenna made of aluminum rods [Fig. 7(a)].

The UAV positioning takes advantage of a real-time kinematic (RTK) receiver, namely a u-blox NEO-M8P, which provides time-stamped position data with a horizontal position accuracy of about 2.5 cm [41]. The vertical accuracy of single-frequency RTK systems is generally twice the horizontal one. As stated in the introduction, the operating frequency was 750 MHz, hence the adopted hardware guaranties about $\lambda/8$ of position accuracy (worst case). It should be mentioned that in standard NF measurements, a position accuracy of $\lambda/100$ to $\lambda/50$ is suggested [13, p. 24] to achieve maximum accuracy. Therefore, a nonnegligible level of uncertainty will be expected in the measured data. Nonetheless, we decided

---

[2] Registered trademark.

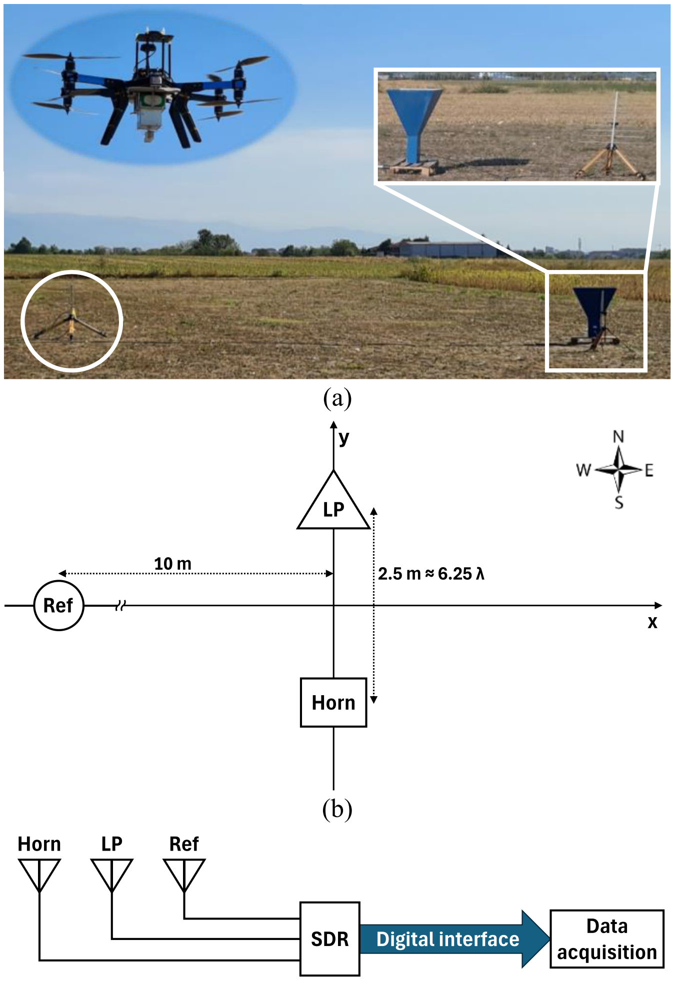
(a)

(b)

(c)

Fig. 7. (a) Picture of the UAV (top left), the array (right), and the reference antenna (bottom left). (b) Nominal antenna arrangement on the field seen from above (compass cross indicating the cardinal directions). (c) Connection scheme.

to work in these challenging conditions to test the overall measurement procedure.

The UAV attitude is measured through the flight controller's inertial measurement unit (IMU). Time-stamped orientation data are used to compute the position of the probe phase center (input for the NFT) using knowledge of the UAV position and the probe location in the UAV frame. It should be noted that standard IMUs generally provide accuracy of a few degrees.

It should be pointed out that the probe pattern is significantly directive at 750 MHz, with nulls at 62° from nadir and a 11-dB drop at 45°. This behavior limits the angular validity region of the NFT and highlights the need to perform probe compensation.

### B. AUT

The proposed EM-aware path was tested along with the SDR measurement setup in outdoor environment.

Absence of RF interference within the receiver bandwidth (200 kHz, Section III) was verified in the measurement field. This condition meets the requirement of a SKA station, which is located in a radio quiet zone to minimize RF interference issues [42]. However, it is worth mentioning that signal processing capabilities of SDR-based setups could be exploited to deal with interfering signals.

TABLE I
MEASURED COORDINATES OF THE ELEMENTS

| | x (mm) | y (mm) | z (mm) |
|---|---|---|---|
| Log-periodic | +55 | +1255 | +19 |
| Horn | −71 | −1256 | +11 |
| Reference | −9927 | +1178 | +190 |

To perform a horizontal planar NF flight at a sufficiently high altitude, a large AUT on the ground is needed to produce a reasonably large Fraunhofer distance. For this reason, we used a two-element array consisting of a PMM LP-02 log-periodic antenna [43] and an Orbit/FR AL-2308-0.75-N standard-gain horn operating in the range 0.75–1.2 GHz. The array elements were deployed along their *E*-plane, pointing toward zenith [Fig. 7(b)]. The log-periodic and horn antennas were mounted over a wooden tripod and a pallet, respectively. The log-periodic antenna had a maximum width of 900 mm and a height of 1093 mm. The horn had an aperture of 800 × 600 mm and a height of 1115 mm. The center-to-center distance between the two elements is 2514 mm. Hence, the largest dimensions of the array are 3264 mm (width) and 1115 mm (height). This implies that the FF region starts at about 53 m from the AUT. The reference antenna consisted in an additional log-periodic antenna placed at approximately 10 m from the array. Any other scattering object was farther than 50 m from the antennas.

The position of the elements was determined with the RTK receiver of the UAV and is reported in Table I. The adopted local reference system is such that the $x$-axis points toward East, while the $y$-axis points toward North and lies in the common *E*-plane. The $z$-axis completes the right-handed triplet and points toward zenith. Each array element was connected to a channel of the SDR through coaxial cables [Fig. 7(c)].

The test conditions described above (receiving AUT, antenna orientation, RF interference, CW test signal) are consistent with those of an in situ measurement of a SKA station [6], [44], with difference that the operating frequency of 750 MHz challenges the positioning accuracy of the source.

### C. Phase Retrieval

The phase measurement is based on IEEE standard [7, pp. 91–92], with the difference that the source and the reference antenna move relative to each other.

The phase of the received signal at the reference antenna port can be expresses, based on Friis transmission equation, as

$$\varphi_r(\underline{r}) = \varphi_s(\underline{r}) - k d_{sr}(\underline{r}) + \angle\langle \hat{p}_r(\hat{r}), \hat{p}_s(\hat{r}, \underline{\psi})\rangle \tag{6}$$

where $\varphi_s$ is the phase of the transmitted signal (unknown), $k$ is the wavenumber, and $d_{sr}$ is the distance between the UAV and the reference antenna, whose position is arbitrary. The aforementioned quantities depend on the position vector of the UAV in the local reference system, $\underline{r}$. The symbol $\angle$ denotes the phase of a complex number. The hat symbol ˆ denotes unit vectors. $\hat{p}_r$ and $\hat{p}_s$ are the polarization unit vectors of the reference antenna and the UAV-mounted one, respectively, ($\hat{p} = \underline{E}/|\underline{E}|$, where $\underline{E}$ is the electric field vector). Both $\hat{p}_r$ and $\hat{p}_s$ depend on the unit vector of the UAV position, whereas $\hat{p}_s$ also depends on the UAV attitude, defined by the angles $\underline{\psi} = (\alpha, \beta, \gamma)$ (yaw, pitch, and roll). For each sample, $\hat{p}_r$ and $\hat{p}_s$ are evaluated from lookup tables of UAV source and reference antenna radiation patterns.

The NFT requires information of the phase of the transmission coefficient between source and AUT, $\Delta\varphi_{as}$. Such quantity can be written as

$$\Delta\varphi_{as} = \varphi_a - \varphi_s \tag{7}$$

where $\varphi_a$ is the phase of the signal measured with the SDR at the AUT port.

The phase term $\varphi_s$ can be derived from (6) using $\varphi_r$ and $\underline{r}$, both measured quantities, and knowledge of source and reference antenna polarization vectors. By substituting $\varphi_s$ in (7), we can obtain $\Delta\varphi_{as}$ through the following equation:

$$\Delta\varphi_{as}(\underline{r}) = \varphi_a^m(\underline{r}) - \varphi_r^m(\underline{r}) - kd_{sr}(\underline{r}) + \angle\langle\hat{p}_r(\hat{r}), \hat{p}_s(\hat{r}, \underline{\psi})\rangle \tag{8}$$

where the subscripts $a$, $s$, and $r$ denote the AUT, the UAV, and the reference antenna, respectively; and the superscript $m$ denotes measured quantities.

It should be noted that $\varphi_a^m$ and $\varphi_r^m$ are streamed through the digital interface of the SDR as time series. The time-stamped UAV data (position and attitude) are then linearly interpolated into the SDR timestamps to obtain a consistent dataset.

## V. RESULTS

### A. NF Data

The EM-aware path was generated as described in Section II on the base of the nominal array morphology and programmed as the mission for the UAV. The flight plan consisted of 350 waypoints within a square flat area of 900 m$^2$ at the nominal height of 4 m (Fig. 8). Such a scanning should in principle provide a validity angle of 75° for the NFT; however, the expected value is limited to about 45° due to the sharp probe pattern (Section IV-A). The flight duration was 10 min. The measured path is slightly different from the programmed one in Fig. 3 because of wind phenomena and real performance of the UAV navigation system. However, as mentioned above, such measured path is known with the accuracy of the RTK GPS.

As already stated in the introduction, in addition to the EM-aware flight we also performed a standard $\lambda/2$ planar NF scan and a direct FF measurement for more comparisons. The raster consisted in 51 equally spaced horizontal scans parallel to the $y$-axis, covering a reduced area of 100 m$^2$ with 0.2 m of line spacing and 4 m of flying height. Its limited 10-m side length was chosen to provide limit the flight duration to 15 min. A validity angle of 45° for the NFT is expected for the raster regardless of the probe pattern.

During all the flights, the programmed UAV heading coincided with the north direction, that is, the onboard dipole axis always lied in the $yz$ plane with small variations mainly dependent on the wind. This strategy allows sampling the $y$-component of the AUT electric field.

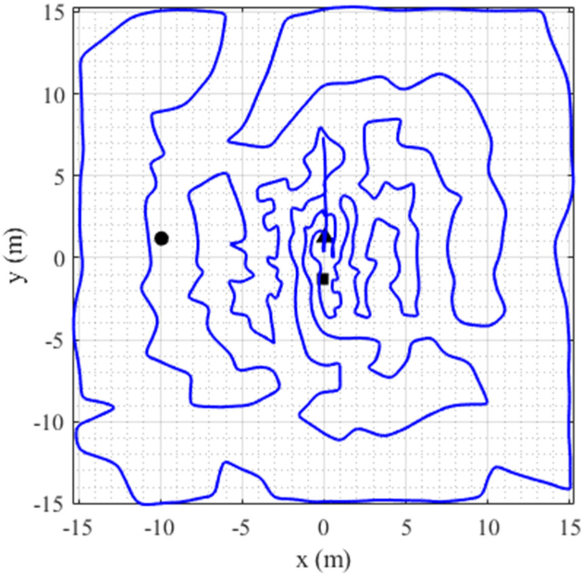

Fig. 8. Measured EM-aware path (solid line) above the array. Elements represented in their real position (Table I). Reference antenna (circle), horn (square), and log-periodic antenna (triangle).

The average UAV altitude during the EM-aware path and the raster was approximately 3.5 and 3.2 m from the top of the AUT, respectively. The UAV relies on the barometric sensor to control the altitude, this explains the different flying heights; nevertheless, the accurate RTK measured altitude is available in postprocessing. The error of the barometric sensor forced us to remain at a safe distance of about 3 m from the top of the AUT. This region corresponds to the radiating NF for both the elements and the whole array. The average and maximum UAV velocity were approximately 0.6 and 1.2 m/s.

The raster is discussed at first due to its ease of interpretation. The received power (normalized to its maximum) measured during a section of the flight at the horn channel is reported in Fig. 9 (orange line). The curve is roughly characterized by a repetition of positive and negative peaks having a periodicity in accordance with the consecutive UAV scans, that is, positive peak occurring when the UAV is at the minimum distance from the horn. The predicted dynamic range of 70 dB is confirmed. The blue dashed line of Fig. 9 shows the simulated response assuming a highly simplified model, in which the received power is computed under FF hypothesis through the Friis equation (i.e., using knowledge of the UAV position and orientation and the simulated AUT and test-source patterns) [3]. In particular, an electromagnetic model was set up for each involved antenna, that is, the array elements, the phase-reference, and the UAV-mounted dipole. Owing to the large distance between the array elements and their reasonably high directivity, each antenna was individually simulated in free space.

Considering samples above the threshold of −30 dB in Fig. 9, the discrepancy is within 1.7 dB. It should be pointed out that such a simplified simulation only aims at estimating

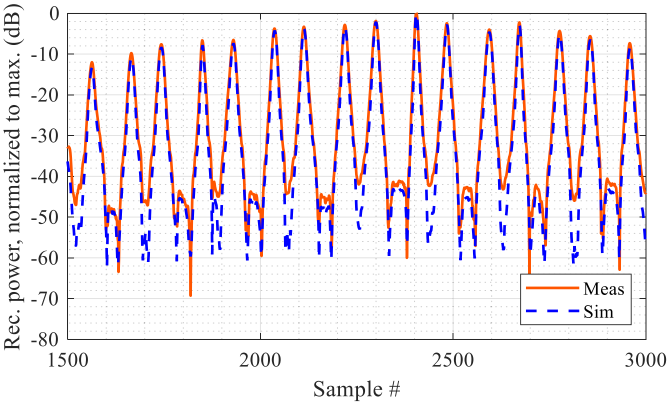

Fig. 9. Raster flight: normalized measured (orange) and simulated (blue dashed) power received at the horn port during a section of 16 consecutive passes.

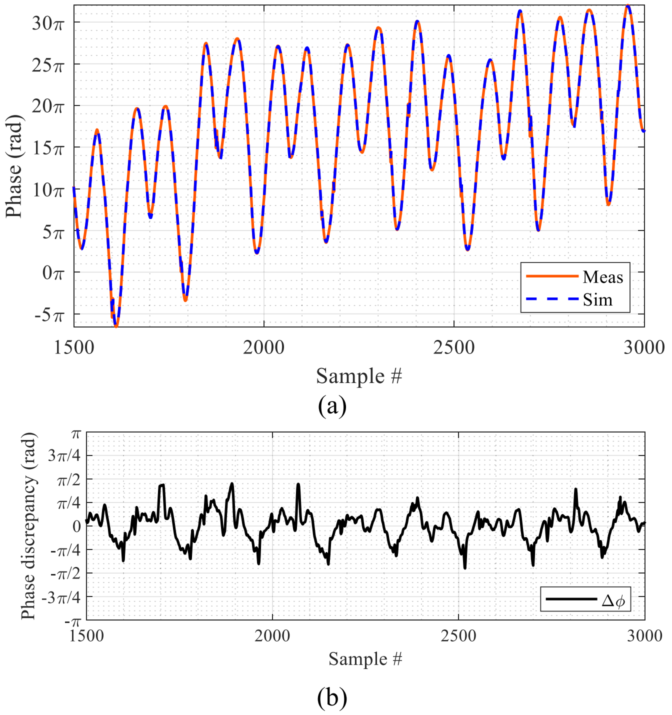

(a)

(b)

Fig. 10. Raster flight. (a) Retrieved (orange) and simulated (blue dashed) phase at the horn port during 16 consecutive passes. (b) discrepancy between measured and simulated phase.

the required dynamic range and the roughly expected response.

To further validate the measurements, a full-wave simulation was performed with CST Microwave Studio.[2] The model included both the horn and the UAV with the measured path and attitude, and the complex transmission coefficient was simulated. Owing to the high computational load, only small portions of the flight were simulated, showing a maximum discrepancy of 1.5 dB.

Fig. 10(a) shows, for the same portion of the raster flight, the measured and simulated phase traces at the horn channel after the retrieval process through the reference antenna (orange and blue dashed curves, respectively). Fig. 10(b) shows the discrepancy between simulated and measured response. It should be noted that large values of discrepancies arise when the received power at the horn channel or the reference antenna channel drops close to the noise floor of the receiver. In fact, considering only the samples with an acceptable signal to noise ratio (SNR); that is, above −60 dB (relative to maximum power of received signal), the discrepancy between measured and simulated phase exhibits a standard deviation of $35^\circ = 7\pi/36$ rad. The latter is equivalent to a displacement of

$$d_{\text{eq}} = \frac{7\pi}{36 k_{wf}} \approx 4 \text{ cm} \tag{9}$$

where $k_{wf}$ is the wavenumber at the working frequency (750 MHz). Hence, the phase discrepancy is consistent with the position accuracy of both the UAV and the array elements. The contribution of the SDR already mentioned in Section III (0.3°) is instead negligible with respect to the observed 35°.

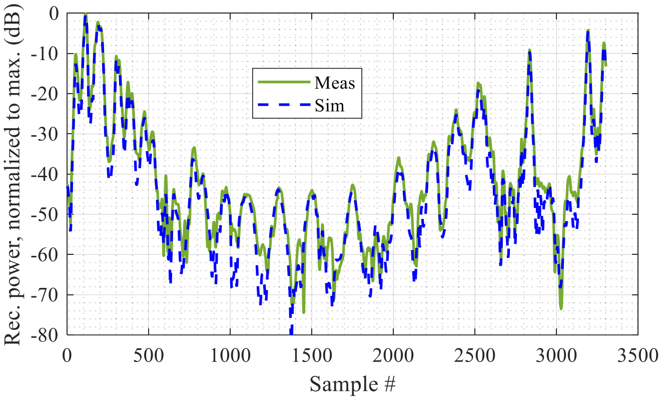

Fig. 11. EM-aware path: normalized measured (green) and simulated (blue dashed) power received at the horn port during the whole flight.

It should be also noted that the phase discrepancy of Fig. 10(b) is characterized by periodic fluctuations of about $\pm\pi/4$ rad (which corresponds to an equivalent length of about 5 cm), having the same periodicity as both the phase diagram of Fig. 10(a) and the power diagram of Fig. 9. For this reason, the discrepancy can be partially interpreted as a systematic error ascribable to intrinsic uncertainty of the RTK and residual positioning errors of the antennas on the ground. The effect of such a significant nonrandom error on the transformed data will be discussed in Section V-B.

As far as the EM-aware path is concerned, Fig. 11 reports the measured and simulated received power (normalized to their maxima) at the horn channel (green and blue dashed, respectively). Starting and arrival waypoints are located over the array, as can be deduced from local maxima of the traces. A remarkable dynamic range of 80 dB was measured during the whole flight; the higher value, with respect to the raster, arises from the larger covered area that implies both a higher free-space path loss and a lower probe gain in the AUT direction.

The measured and simulated phase traces are shown in Fig. 12(a) (green and blue dashed, respectively). The difference between the curves is shown in Fig. 12(b), solid/dashed line representing the samples above above/below −60 dB. The standard deviation of the phase discrepancy for the EM-aware path is 45° (i.e., ∼5 cm of equivalent distance). This result is consistent with the raster case; however, the higher value of the EM-aware path arises from the increased path tortuosity

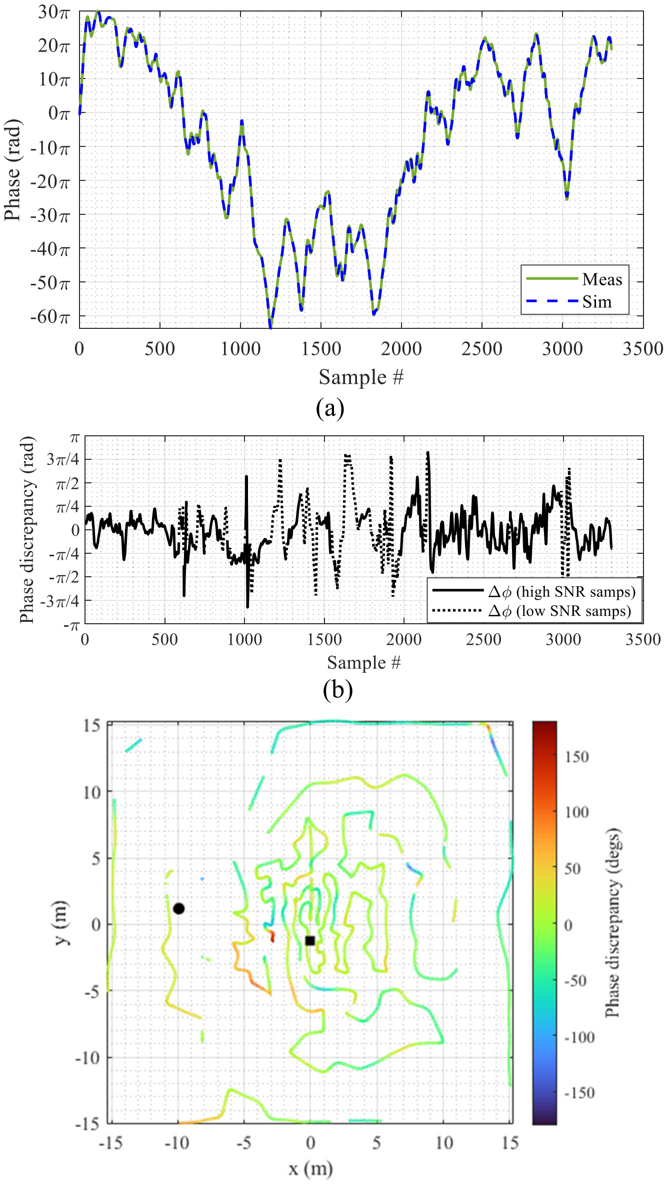

(a)

(b)

(c)

Fig. 12. EM-aware path. (a) Retrieved (green) and simulated (blue dashed) phase at the horn port during the whole flight. (b) Discrepancy between measured and simulated phase, solid/dotted line representing samples above/below $-60$ dB. (c) 2-D colormap of the phase discrepancy on top of the flight path (only samples above $-60$ dB), square/circle marker indicating the horn/reference antenna.

that entails frequent variations in the UAV attitude, which in turn affects the accuracy of the reconstruction of the probe's phase center position (Section IV-A). Such a phenomenon is visible in Fig. 12(c) where the phase discrepancy is reported on top of the flying path: a peak of phase discrepancy was observed when the UAV was approximately between the horn (square marker) and the reference antenna (circle). In this case an abrupt flight maneuver is the cause of the peak discrepancy.

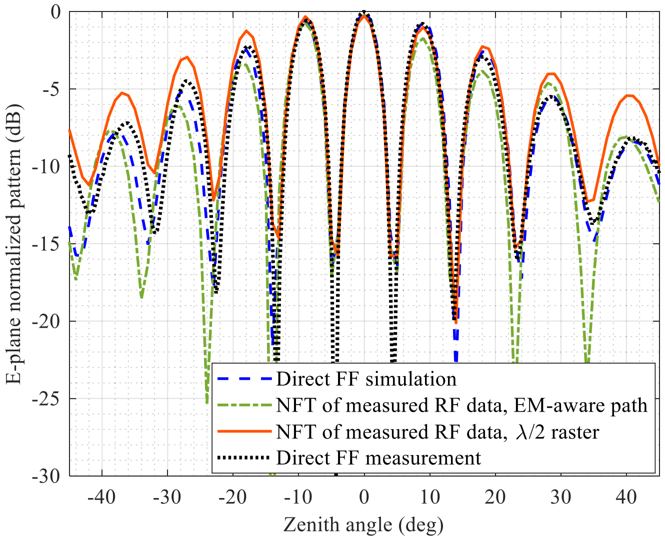

Fig. 13. Normalized array pattern, $E$-plane cut. Direct FF simulation (blue dashed), NFT of the measured RF data during the EM-aware path (green dash-dotted), NFT of the measured RF data during the $\lambda/2$ raster (orange solid), and direct FF measurement (black dotted).

### B. FF Pattern

The radiation pattern is computed from the NF measurements applying the inverse source NFT of Section II. Samples below the threshold of $-60$ dB are discarded, retaining the samples illustrated in Fig. 12(c). The used SDR-based receiver allows digitizing each element signal and implementing digital beamforming. As reported in Section V-A, radiation patterns of the two array elements (horn and log-periodic antenna) are computed from the NF EM-aware path through the inverse source NFT. The two element patterns are then equalized at zenith (magnitude and phase) and summed together to obtain the beam toward zenith. In this way the possible differences in the gains of the receiver channels are calibrated out.

Fig. 13 shows a comparison of the obtained array patterns on the $E$-plane cut. The NFT output from the EM-aware path (green dash-dotted line) is reported together with the result from the standard raster (orange solid), the direct measurement in FF (black dotted), and a direct FF simulation (full-wave simulation using MoM [36]) (blue dashed). The FF flight only consisted of one scan along the $y$-axis at 60 m height and 3 m/s of speed, to measure the $E$-plane cut. Such flight lasted 3 min. The FF measurement is a consolidated procedure [3], [6], [40] with an error in the order of 0.5 dB. We will use it as reference data in the following discussion.

Grating lobes are present due to the large spacing between the two elements ($6.27\lambda$). All the curves are in good agreement in the main lobe and first grating lobes regions (at $\pm 9^{\circ}$), including the position of the first nulls (at $\pm 4.5^{\circ}$ and $\pm 13^{\circ}$). The dispersion of the curves increases approaching the NFT validity boundary (at $\pm 45^{\circ}$ from zenith) due to the progressively lower probe gain toward the AUT and therefore a less efficient compensation; this is particularly evident in the raster since the UAV flew at a lower altitude. However, the overall accordance of the result from the EM-aware path (green dash-dotted) with direct FF curves (blue dashed and black dotted) is remarkable. With reference to Fig. 13, the good agreement between direct FF measurement and direct FF simulation demonstrates the accuracy of the EM model of the AUT.

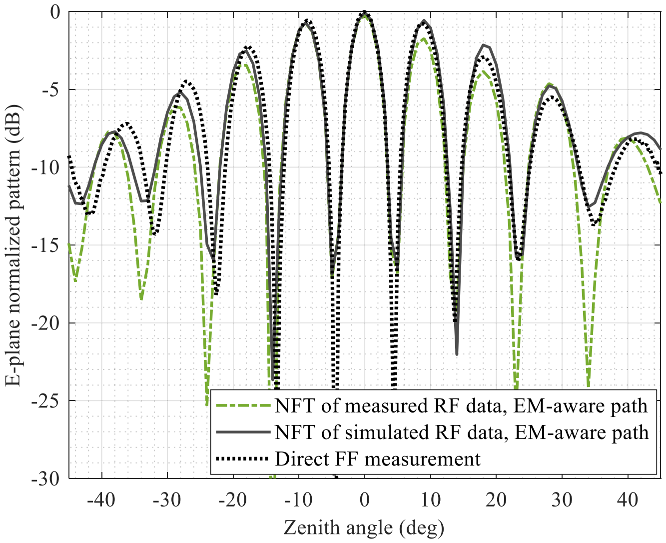

Fig. 14. Comparison between simulated array pattern, *E*-plane cut. Direct FF measurement (black dotted), NFT of the measured RF data during the EM-aware path (green dash-dotted), NFT of the simulated RF data along the actual EM-aware path (gray solid).

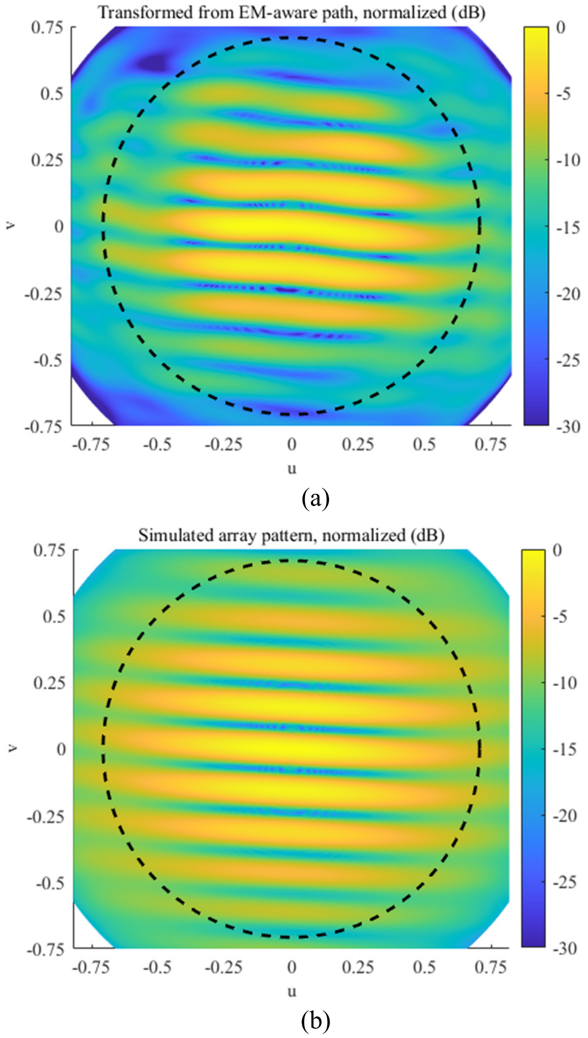

Fig. 15. 2-D chart in the *uv* plane of (a) transformed array pattern from EM-aware measurement. (b) Simulated FF array pattern. The dashed black circumference delimits the angular validity of the NFT from the EM-aware measurement (45°).

TABLE II

DURATION OF DIFFERENT SCAN STRATEGIES

| | Duration (minutes) | Nominal angular coverage from zenith |
|---|---|---|
| EM-aware path | 10 | 75° (900 $m^2$ area) |
| $\lambda/2$ raster | > 100 | 75° (900 $m^2$ area) |
| $\lambda/2$ spiral | 80 | 75° |
| Reduced $\lambda/2$ raster | 15 | 45° (100 $m^2$ area) |
| FF, 2 main cuts | 5 | 75° |
| FF, full pattern | > 100 | 75° |

The residual discrepancy is related to absence of the soil in EM model.

In order to explain the discrepancy between direct FF data and the measured EM-aware result, we performed a NF simulation of the AUT along the actual EM-aware path and applied the NFT. In this way, we removed the uncertainty of the RF data generated by the measurement equipment. The NFT result of such data is reported in Fig. 14 with gray solid curve. The black dotted curve corresponds again to the direct FF measurement (same as in Fig. 13). The gray solid curve (NFT of simulated RF data) shows a better agreement to the FF measurement with respect to the original green one (NFT of measured RF data). This confirms that the error on the EM-aware measured curve is mainly related to the errors in the acquired RF data. As discussed in Section V-A, such errors are mainly related to the uncertainty of the differential GPS. The residual discrepancy of the gray curve is still related to absence of the soil in EM model.

Though the FF measurement provides the best accuracy level, it should be remarked that within a flight duration comparable with the EM-aware path, the direct FF measurement only returns a small number of cuts while the NF approach allows measuring the full radiation pattern.

For a complete comparison over the full azimuthal angle, 2-D maps of the transformed and simulated array patterns are reported in Fig. 15(a) and (b), respectively. The dashed black circle represents the NFT angular validity (45° from zenith). The general shape including grating lobes is predicted; however, the suboptimal probe pattern (Section V-A) and the rough adopted probe compensation do not allow to fully reconstruct the FF array pattern in the proximity of the angular validity threshold. The mean absolute error [see (5)] inside the angular validity range is 2.95 dB and is mainly caused by small discordances in the positions of the sharp nulls. The main beam and the sidelobes are not perfectly parallel to the *x*-axis (i.e., $\phi = 0°$) but show a small rotation (approximately in the plane $\phi = -3°$). This is because the elements are not located exactly on the *y*-axis ($x = 0$ m) but have a little displacement along the *x*-axis (less than $0.2\lambda$, Table I).

Finally, the durations of different flight strategies are summarized in Table II.

## VI. CONCLUSION

An electromagnetics-aware path strategy for NF antenna measurements was implemented in a UAV-based scenario.

Using only knowledge of the AUT bulk spatial occupancy, the EM-aware path was computed and tested outdoor. The high dynamic signals were acquired using a commercial SDR with multichannel coherency and scaling possibility. The proposed strategy drastically reduces the scanning time required in UAV-based planar NF acquisitions. Moreover, it allows a complete control of the truncation error and its relationship with the path length can be numerically determined in advance.

It is worth mentioning that a more sophisticated path-generation algorithm could enforce additional constraints to improve the overall accuracy; for example, avoiding excessively sharp curves or intercepting probe nulls. The proposed method can be also generalized to arbitrary measurement surfaces (nonplanar) in scenarios involving standard positioners.

The presented results show one of the possible measurement configurations that can be explored with an UAV-based NF setup. The method has been presented for planar scan of an antenna array pointing at zenith. However, it can deal with arbitrary distribution of sources and arbitrary shapes of the available test area, by inserting an appropriate sampling of the source and the test regions in (1). For example, elongated structures such as leaky coaxial cables can be handled by the algorithm considering $L$ source points $\underline{r}'_\ell$ positioned along the cables. Path reduction with respect to standard raster or cylindrical scan should be assessed in real scenarios. Similar considerations apply to distributed sources.

Despite the uncertainty of the UAV positioning system, the obtained measurement accuracy is acceptable. The effect of the phase error cannot be easily quantified as it depends on its distribution; therefore, the method was validated through a cross comparison between direct FF measurement, direct FF simulation, and NFT of the simulated RF data in NF. The consistency between the data confirms that the uncertainty of the EM-aware measurement mainly originates from errors on the acquired RF data, in which the phase uncertainty is not negligible.

The positive results achieved with this proof-of-concept encourage further activities in more challenging configurations; that is, on larger arrays, different AUTs, sparse sources, other pointing directions, other scan surfaces (e.g., vertical, hemispherical, cylindrical), other feeding schemes, and more complex environments (presence of scatterers).

As far as the experimental setup is concerned, other optimized scanning strategies such as [45] could be also considered owing to the generality of the programmable paths on the UAV.

Our findings can be further explored using more accurate six-degrees-of-freedom positioning solutions (i.e., for both probe position and orientation) integrated into the flight control loop, such as camera-based tracking systems [46], advanced IMUs [47], and/or laser trackers [15]; these devices could allow the implementation of the EM-aware scanning method in the reactive NF and the usage of all the resources of modern SDRs working in C-band to operate at higher frequencies with respect to the presented activity. The integration of UAVs and SDRs can, in perspective, provide the wireless communication industries advanced tools to perform MIMO testing and OTA characterization of active antenna systems in highly interfered environments exploiting signal processing capabilities of SDRs.

## ACKNOWLEDGMENT

The authors acknowledge Dr. Chiara Mello, Politecnico di Torino, Turin, Italy, for her valuable work concerning the SDR software development.

## REFERENCES

[1] A. Salari and D. Erricolo, “Unmanned aerial vehicles for high-frequency measurements: An accurate, fast, and cost-effective technology,” *IEEE Antennas Propag. Mag.*, vol. 64, no. 1, pp. 39–49, Feb. 2022, doi: 10.1109/MAP.2021.3061026.

[2] O. Breinbjerg et al., “Antenna measurement challenges and opportunities,” *Rev. Electromagn.*, vol. 2, pp. 1–49, Dec. 2023, doi: 10.53792/roe/2023/23003.

[3] G. Virone et al., “Antenna pattern verification system based on a micro unmanned aerial vehicle (UAV),” *IEEE Antennas Wireless Propag. Lett.*, vol. 13, pp. 169–172, 2014, doi: 10.1109/LAWP.2014.2298250.

[4] C. Culotta-López et al., “On the uncertainty sources of drone-based outdoor far-field antenna measurements,” in *Proc. Antenna Meas. Techn. Assoc. Symp. (AMTA)*, Daytona Beach, FL, USA, Oct. 2021, pp. 1–6, doi: 10.23919/AMTA52830.2021.9620638.

[5] J. L. Salazar-Cerreno, S. S. Jehangir, N. Aboserwal, A. Segales, and Z. Qamar, “An UAV-based polarimetric antenna measurements for radar and communication systems from 3 GHz to 32 GHz,” in *Proc. IEEE Conf. Antenna Meas. Appl. (CAMA)*, Antibes Juan-les-Pins, France, Nov. 2021, pp. 55–60, doi: 10.1109/CAMA49227.2021.9703660.

[6] F. Paonessa et al., “SKA-low prototypes deployed in Australia: Synoptic of the UAV-based experimental results,” *Radio Sci. Lett.*, vol. 2, pp. 1–12, Sep. 2020, doi: 10.46620/20-0021.

[7] *IEEE Recommended Practice for Antenna Measurements*, IEEE Standard 149-2021, Feb. 18, 2022, pp. 1–207, doi: 10.1109/IEEESTD.2022.9714428.

[8] T. Bourke, “Advancing astrophysics with the square kilometre array,” *Pos Proc. Sci.*, vol. 215, p. 174, 2015, doi: 10.22323/1.215.0174.

[9] M. P. van Haarlem et al., “LOFAR: The low-frequency array,” *Astron. Astrophys.*, vol. 556, p. A2, Aug. 2013, doi: 10.1051/0004-6361/201220873.

[10] G. Virone et al., “Measurement of the LOFAR-HBA beam patterns using an unmanned aerial vehicle in the near field,” *J. Astronomical Telescopes, Instrum., Syst.*, vol. 8, no. 1, Nov. 2021, Art. no. 011005, doi: 10.1117/1.jatis.8.1.011005.

[11] G. W. Kant, P. D. Patel, S. J. Wijnholds, M. Ruiter, and E. van der Wal, “EMBRACE: A multi-beam 20,000-element radio astronomical phased array antenna demonstrator,” *IEEE Trans. Antennas Propag.*, vol. 59, no. 6, pp. 1990–2003, Jun. 2011, doi: 10.1109/TAP.2011.2122233.

[12] S. A. Torchinsky et al., “Characterization of a dense aperture array for radio astronomy,” *Astron. Astrophys.*, vol. 589, p. A77, May 2016, doi: 10.1051/0004-6361/201526706.

[13] *IEEE Recommended Practice for Near-Field Antenna Measurements*, IEEE Standard 1720-2012, Dec. 2012, pp. 1–102, doi: 10.1109/IEEESTD.2012.6375745.

[14] M. García-Fernández et al., “Antenna diagnostics and characterization using unmanned aerial vehicles,” *IEEE Access*, vol. 5, pp. 23563–23575, 2017, doi: 10.1109/ACCESS.2017.2754985.

[15] S. Punzet et al., “Fully coherent UAV-based near-field measurement and transformation of the S67-15 m ground station antenna at the German space operations center in Weilheim,” in *Proc. 16th Eur. Conf. Antennas Propag. (EuCAP)*, Madrid, Spain, Mar. 2022, pp. 1–5, doi: 10.23919/EuCAP53622.2022.9769018.

[16] R. A. M. Mauermayer and J. Kornprobst, “A cost-effective tethered-UAV-based coherent near-field antenna measurement system,” *IEEE Open J. Antennas Propag.*, vol. 3, pp. 984–1002, 2022, doi: 10.1109/OJAP.2022.3198269.

[17] L. Ciorba et al., “Large horizontal near-field scanner based on a non-tethered unmanned aerial vehicle,” *IEEE Open J. Antennas Propag.*, vol. 3, pp. 568–582, 2022, doi: 10.1109/OJAP.2022.3173741.

[18] F. Paonessa, G. Virone, P. Bolli, G. Addamo, S. Matteoli, and O. A. Peverini, “UAV-based antenna measurements: Improvement of the test source frequency behavior,” in *Proc. IEEE Conf. Antenna Meas. Appl. (CAMA)*, Västerås, Sweden, Sep. 2018, pp. 1–3, doi: 10.1109/CAMA.2018.8530506.

[19] J. Li, J. Zhou, S. Yong, Y. Liu, and V. Khilkevich, "Automatic sparse ESM scan using Gaussian process regression," in *Proc. IEEE Int. Symp. Electromagn. Compat. Signal/Power Integrity (EMCSI)*, Reno, NV, USA, Jul. 2020, pp. 671–675, doi: 10.1109/EMCSI38923.2020.9191463.

[20] B. Fuchs and A. G. Polimeridis, "Reduced order models for fast antenna characterization," *IEEE Trans. Antennas Propag.*, vol. 67, no. 8, pp. 5673–5677, Aug. 2019.

[21] O. M. Bucci, C. Gennarelli, and C. Savarese, "Representation of electromagnetic fields over arbitrary surfaces by a finite and nonredundant number of samples," *IEEE Trans. Antennas Propag.*, vol. 46, no. 3, pp. 351–359, Mar. 1998, doi: 10.1109/8.662654.

[22] Q. Gueuning, C. Craeye, E. de Lera Acedo, and A. K. Brown, "Improving the accuracy of a model-based approach for the near-field measurement of antenna arrays with UAVs," in *Proc. 17th Eur. Conf. Antennas Propag. (EuCAP)*, Florence, Italy, Mar. 2023, pp. 1–3, doi: 10.23919/EuCAP57121.2023.10133185.

[23] O. Neitz, R. A. M. Mauermayer, Y. Weitsch, and T. F. Eibert, "A propagating plane-wave-based near-field transmission equation for antenna gain determination from irregular measurement samples," *IEEE Trans. Antennas Propag.*, vol. 65, no. 8, pp. 4230–4238, Aug. 2017, doi: 10.1109/TAP.2017.2712180.

[24] L. Ciorba, F. Paonessa, M. Righero, G. Giordanengo, G. Virone, and G. Vecchi, "Radiation physics allows ten-fold optimization of UAV near-field scanning," in *Proc. 17th Eur. Conf. Antennas Propag. (EuCAP)*, Florence, Italy, Mar. 2023, pp. 1–4, doi: 10.23919/EuCAP57121.2023.10133100.

[25] F. Paonessa, L. Ciorba, M. Righero, G. Giordanengo, G. Virone, and G. Vecchi, "SDR-enabled near-field measurements with UAVs," in *Proc. IEEE Conf. Antenna Meas. Appl. (CAMA)*, Genoa, Italy, Nov. 2023, pp. 159–160, doi: 10.1109/CAMA57522.2023.10352846.

[26] R. T. Sanchez, M. S. Castaner, and L. J. Foged, "A referenceless antenna measurement system based on software-defined radio [measurements corner]," *IEEE Antennas Propag. Mag.*, vol. 62, no. 5, pp. 108–118, Oct. 2020, doi: 10.1109/MAP.2020.3012897.

[27] R. T. Sánchez, M. S. Castañer, and L. J. Foged, "Use of software defined radio receivers for antenna measurements," in *Proc. Photon. Electromagn. Res. Symp.-Spring (PIERS-Spring)*, Rome, Italy, Jun. 2019, pp. 1862–1869, doi: 10.1109/PIERS-Spring46901.2019.9017439.

[28] J. L. A. Quijano and G. Vecchi, "Field and source equivalence in source reconstruction on 3D surfaces," *Prog. Electromagn. Res.*, vol. 103, pp. 67–100, 2010, doi: 10.2528/PIER10030309.

[29] S. Rao, D. Wilton, and A. Glisson, "Electromagnetic scattering by surfaces of arbitrary shape," *IEEE Trans. Antennas Propag.*, vol. AP-30, no. 3, pp. 409–418, May 1982, doi: 10.1109/TAP.1982.1142818.

[30] G. H. Golub and C. F. van Loan, *Matrix Computations*, 3rd d., Baltimore, MD, USA: Johns Hopkins Univ., 1996.

[31] T. F. Chan, "Rank revealing QR factorizations," *Linear Algebra Appl.*, vols. 88–89, pp. 67–82, Apr. 1987.

[32] M. A. Qureshi, C. H. Schmidt, and T. F. Eibert, "Efficient near-field far-field transformation for nonredundant sampling representation on arbitrary surfaces in near-field antenna measurements," *IEEE Trans. Antennas Propag.*, vol. 61, no. 4, pp. 2025–2033, Apr. 2013, doi: 10.1109/TAP.2012.2231932.

[33] G. Leone, R. Moretta, and R. Pierri, "Dimension and sampling of the near-field and its intensity over curves," *IEEE Open J. Antennas Propag.*, vol. 3, pp. 412–424, 2022, doi: 10.1109/OJAP.2022.3166633.

[34] F. D'Agostino, F. Ferrara, C. Gennarelli, R. Guerriero, S. McBride, and M. Migliozzi, "Fast and accurate antenna pattern evaluation from near-field data acquired via planar spiral scanning," *IEEE Trans. Antennas Propag.*, vol. 64, no. 8, pp. 3450–3458, Aug. 2016, doi: 10.1109/TAP.2016.2576483.

[35] A. C. Newell, "Error analysis techniques for planar near-field measurements," *IEEE Trans. Antennas Propag.*, vol. 36, no. 6, pp. 754–768, Jun. 1988, doi: 10.1109/8.1177.

[36] M. Li, M. A. Francavilla, R. Chen, and G. Vecchi, "Wideband fast kernel-independent modeling of large multiscale structures via nested equivalent source approximation," *IEEE Trans. Antennas Propag.*, vol. 63, no. 5, pp. 2122–2134, May 2015, doi: 10.1109/TAP.2015.2402297.

[37] S. Pivnenko et al., "Comparison of antenna measurement facilities with the DTU-ESA 12 GHz validation standard antenna within the EU antenna centre of excellence," *IEEE Trans. Antennas Propag.*, vol. 57, no. 7, pp. 1863–1878, Jul. 2009, doi: 10.1109/TAP.2009.2021934.

[38] Ettus Res. (2019). *USRP X300 and X310 Spec Sheet*. Accessed: Jan. 2024. [Online]. Available: https://www.ettus.com/wp-content/uploads/2019/01/X300_X310_Spec_Sheet_9.20.2022.pdf

[39] Ettus Res. (2021). *TwinRX Datasheet*. Accessed: Jan. 2024. [Online]. Available: https://www.ettus.com/wp-content/uploads/2021/06/TwinRX_Datasheet.pdf

[40] F. Paonessa et al., "Design and verification of a $Q$-band test source for UAV-based radiation pattern measurements," *IEEE Trans. Instrum. Meas.*, vol. 69, no. 12, pp. 9366–9370, Dec. 2020, doi: 10.1109/TIM.2020.3031127.

[41] U-blox. *NEO-M8P Datasheet*. Accessed: Jan. 2024. [Online]. Available: https://content.u-blox.com/sites/default/files/NEO-M8P_DataSheet_UBX-15016656.pdf

[42] C. Wilson, K. Chow, L. Harvey-Smith, B. Indermuehle, M. Sokolowski, and R. Wayth, "The Australian radio quiet zone—Western Australia: Objectives, implementation and early measurements," in *Proc. Int. Conf. Electromagn. Adv. Appl. (ICEAA)*, Cairns, QLD, Australia, Sep. 2016, pp. 922–923, doi: 10.1109/ICEAA.2016.7731554.

[43] Narda. *LP-02 Datasheet*. Accessed: Jan. 2024. [Online]. Available: https://www.narda-sts.it/download/745/

[44] E. de Lera Acedo et al., "SKA aperture array verification system: Electromagnetic modeling and beam pattern measurements using a micro UAV," *Exp. Astron.*, vol. 45, no. 1, pp. 1–20, Mar. 2018, doi: 10.1007/s10686-017-9566-x.

[45] F. Bevilacqua et al., "An effective near-field to far-field transformation with planar spiral scanning for flat antennas under test," *Sensors*, vol. 23, no. 16, p. 7276, Aug. 2023, doi: 10.3390/s23167276.

[46] F. M. Palacios, E. S. E. Quesada, G. Sanahuja, S. Salazar, O. G. Salazar, and L. R. G. Carrillo, "Test bed for applications of heterogeneous unmanned vehicles," *Int. J. Adv. Robotic Syst.*, vol. 14, no. 1, Jan. 2017, Art. no. 1729881416687111, doi: 10.1177/1729881416687111.

[47] Vectornav. *VN-200 GNSS/INS Datasheet*. Accessed: Jan. 2024. [Online]. Available: https://www.vectornav.com/docs/default-source/datasheets/vn-200-datasheet-rev2.pdf?sfvrsn=e1a7b2a0_10

**Lorenzo Ciorba** received the master's degree in mathematical engineering from the Politecnico di Torino, Turin, Italy, in March 2018, with the thesis "Hybrid Antenna Measurement and Simulations" with Prof. G. Vecchi as a Supervisor, and the Ph.D. degree in electrical, electronics and communications engineering from the Politecnico di Turin, in 2022, with the thesis "UAV-based Far-Field and Near-Field Antenna Measurements."

In June 2018, he joined the Applied Electromagnetics Group, Institute of Electronics, Computer and Telecommunication Engineering (IEIIT), Italian National Research Council (CNR), Turin, as a Research Fellow. In August 2023, he joined the Microwave Physics Group, Institute of Applied Physics, University of Bern, Bern, Switzerland, as a Post-Doctoral Researcher. His scientific interests currently include antenna testing, material characterization, and synthetic aperture imaging.

**Fabio Paonessa** (Member, IEEE) received the B.S. and M.S. degrees in biomedical engineering and the Ph.D. degree in electronics engineering from the Polytechnic of Turin, Turin, Italy, in 2008, 2010, and 2017, respectively.

From 2011 to 2012, he was a Research Assistant with the Department of Electronics, Polytechnic of Turin. His activities concerned the design of electronic systems to generate high-intensity focused ultrasounds for sonodynamic therapy. In 2013, he joined the Applied Electromagnetics Group, CNR-IEIIT, Turin, where he became a Researcher in 2018. His current activities include UAV-based characterization of antenna arrays, polarimeters, radar systems, and the design of microwave passive components.

**Marco Righero** received the B.Sc. degree in mathematics for engineering sciences, the M.Sc. degree in mathematical engineering, and the European Ph.D. degree in electronic and communication engineering from the Politecnico di Torino, Turin, Italy, in 2003, 2005, and 2009, respectively.

His main research activity was carried out at the Politecnico di Torino, the University of California at San Diego, La Jolla, CA, USA, and the University College Cork, Cork, Ireland. In 2009, he joined the Department of Electronics, Politecnico di Torino, as a Research Assistant with a fellowship from the Istituto Superiore Mario Boella (ISMB, which is now part of the LINKS Foundation), Turin. Within this project, he received a grant from the Fondazione CRT. In 2010, he started collaborating with the Antenna and EMC Laboratory (LACE), ISMB, Turin, and in 2011, he officially joined the group, where he works on innovative models and efficient methods for the study of electromagnetic propagation in complex media, optimization techniques for antenna arrays synthesis, and antenna measurements.

**Giorgio Giordanengo** received the B.Sc. degree in electronics engineering, the M.Sc. degree in telecommunications engineering, and the Ph.D. degree in information and communications engineering with focus on applied electromagnetics from the Politecnico di Torino, Turin, Italy, in 2006, 2009, and 2016, respectively.

In 2008, as part of his M.S. thesis, he worked with the PLAN Group, University of Calgary, Calgary, AB, in the field of GNSS and jamming. From 2009 to 2011, he was a System Design Engineer with Alenia SIA Spa, Turin, where he worked on the Eurofighter Typhoon navigation sub-system. In 2011, he reached ISMB, and he works on the study and development for RF testing solution on large structures by mixing simulations and measurements. Since 2013, he has been a Senior Researcher at LINKS Foundation, Turin, where he is involved in the design and development of innovative antennas up to Ka-band. He has also experience of antenna testing and measurements (both in anechoic chamber than in outdoor) up to 40 GHz. Finally, he is the co-author of several publications presented in many European and international conferences and a co-inventor of two patents related to the application of microwaves to the agriculture and to the satellite signal tracking by means of electronically steerable antenna.

**Giuseppe Addamo** (Member, IEEE) was born in Messina, Italy, in 1979. He received the Laurea degree (summa cum laude) in electronic engineering and the Ph.D. degree in electronic and communication engineering from the Politecnico di Torino, Turin, Italy, in 2003 and 2007, respectively.

In January 2007, he joined the Istituto di Elettronica e di Ingegneria dell'Informazione e delle Telecomunicazioni (IEIIT), Consiglio Nazionale delle Ricerche (CNR), Turin, as a Research Fellow, and in 2012, he became a Researcher. He holds practical classes in courses on electromagnetic field theory and mathematical analysis at the Politecnico di Torino. His research interests are in the areas of microwave leaky antennas, dielectric radomes, high-power feed systems (e.g., orthomode transducers (OMTs), microwave filters), corrugated horns, frequency-selective surfaces, and large dielectric radomes.

**Giuseppe Vecchi** (Life Fellow, IEEE) received the Laurea and Ph.D. degrees in electronic engineering from the Politecnico di Torino, Turin, Italy, in 1985 and 1989, respectively.

He is a Doctoral research carried out partly at Polytechnic University of NY, Farmingdale, NY, USA. He was a Visiting Scientist with the Polytechnic University of NY from 1989 to 1990, and since 1990, he has been with the Department of Electronics, Politecnico di Torino, where he has been an Assistant Professor, Associate Professor from 1992 to 2000, and Professor. He was a Visiting Scientist with the University of Helsinki, Helsinki, Finland, in 1992, and has been an Adjunct Faculty with the Department of Electrical and Computer Engineering, University of Illinois at Chicago, Chicago, IL, USA, from 1997 to 2011. Since 2015, he has been serving as the Director of the Antenna and EMC Laboratory (LACE), Politecnico di Torino. His current research activities concern analytical and numerical techniques for design, measurement and diagnostics of antennas and devices, medical applications, and imaging.

He is a member of the Board of the European School of Antennas (ESoA) and the IEEE Antennas and Propagation Standard Committee. He has been an Associate Editor for IEEE TRANSACTIONS ON ANTENNAS AND PROPAGATION, the Chairperson of the IEEE AP/MTT/ED Italian joint Chapter, and a member of the IEEE-APS Educational Committee.

**Giuseppe Virone** (Senior Member, IEEE) was born in Turin, Italy, in 1977. He received the Laurea degree (summa cum laude) in electronic engineering, and the Ph.D. degree in electronics and communication engineering from the Politecnico di Torino, Turin, Italy, in November 2001 and 2006, respectively.

He is currently a Senior Researcher with the Istituto di Elettronica e di Ingegneria Informatica e delle Telecomunicazioni (IEIIT), Italian National Research Council (CNR), Turin. He joined IEIIT as a Research Assistant in 2002. He coordinated more than 15 scientific projects funded by both the industry and other scientific research organizations and joined more than 30 research projects as a collaborator. He authored 43 journal papers, 134 conference papers, and three European patents. His activities concern the design, numerical analysis, and characterization of microwave and millimeter passive components for feed systems, antenna arrays, frequency selective surfaces, compensated dielectric radomes, and industrial sensing applications.

Open Access funding provided by 'Consiglio Nazionale delle Ricerche-CARI-CARE-ITALY'
within the CRUI CARE Agreement